

# Luttinger, Peierls or Mott?

## Quantum Phase Transitions in Strongly Correlated 1D Electron–Phonon Systems

Holger Fehske and Georg Hager

**Abstract.** We analyse the complex interplay of charge, spin, and lattice degrees of freedom in one-dimensional electron systems coupled to quantum phonons. To this end, we study generic model Hamiltonians, such as the Holstein models of spinless fermions, the Holstein–Hubbard model and a Heisenberg spin-chain model with magneto-elastic interaction, by means of an unbiased numerical density–matrix renormalisation group technique. Thereby particular emphasis is placed on the Luttinger–liquid charge–density-wave, Peierls–insulator Mott-insulator, and spin–Peierls quantum phase transitions.

### 1.1 Introduction

The way a material evolves from a metallic to an insulating state is one of the most fundamental problems in solid state physics. Apart from band structure and disorder effects, electron–electron and electron–phonon interactions are the driving forces behind metal–insulator transitions in the majority of cases. While the so-called Mott–Hubbard transition [1] is caused by strong Coulomb correlations, the Peierls transition [2] is triggered by the coupling to vibrational excitations of the crystal. Both scenarios compete in a subtle way. As a result, quantum phase transitions (QPT) between insulating phases become possible. Most notably this applies to quasi one-dimensional (1D) materials like conjugated polymers, organic charge transfer salts, ferroelectric perovskites, or halogen-bridged transition metal complexes, which exhibit a remarkably wide range of strengths of competing forces [3, 4]. Moreover, 1D systems are known to be very susceptible to structural distortions.

The challenge of understanding such a kind of metal–insulator or insulator–insulator QPT has stimulated intense work on generic microscopic models of interacting electrons and phonons. In this respect, the 1D Holstein–Hubbard model is particularly rewarding to study [5–10]. It accounts for a tight-binding electron band, a local coupling of the charge carriers to optical phonons, the energy of the phonon subsystem in harmonic approximation, and an intra-site Coulomb repulsion between electrons of opposite spin:

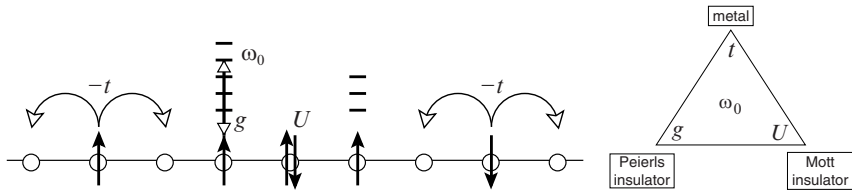


**Fig. 1.1.** The 1D Holstein–Hubbard model (*left panel*) and the competing ground states for the half-filled band case (*right panel*)

$$H = -t \sum_{\langle i,j \rangle \sigma} c_{i\sigma}^\dagger c_{j\sigma} - g\omega_0 \sum_{i\sigma} (b_i^\dagger + b_i) n_{i\sigma} + \omega_0 \sum_i b_i^\dagger b_i + U \sum_i n_{i\uparrow} n_{i\downarrow}. \quad (1.1)$$

Here  $n_{i\sigma} = c_{i\sigma}^\dagger c_{i\sigma}$ , where  $c_{i\sigma}^\dagger$  ( $c_{i\sigma}$ ) creates (annihilates) a spin- $\sigma$  electron at Wannier site  $i$  of a 1D lattice with  $N$  sites, and  $b_i^\dagger$  ( $b_i$ ) are the corresponding bosonic operators for a dispersionsless phonon with frequency  $\omega_0$ .

The physics of the Holstein<sup>1</sup>–Hubbard<sup>2</sup> model is governed by three competing effects: the itinerancy of the electrons ( $\propto t$ ), their on-site Coulomb repulsion ( $\propto U$ ), and the local electron–phonon (EP) coupling ( $\propto g$ ). As the EP interaction is retarded, the phonon frequency ( $\omega_0$ ) defines a further relevant energy scale (see Fig. 1.1). This advises us to introduce besides the adiabaticity ratio,  $\omega_0/t$ , two dimensionless coupling constants

$$u = U/4t \quad \text{and} \quad g^2 = \varepsilon_p/\omega_0 \quad \text{or} \quad \lambda = \varepsilon_p/2t. \quad (1.2)$$

Both Holstein and Hubbard interactions tend to immobilise the charge carriers. Therefore, Peierls insulator (PI) or Mott insulator (MI) states are expected to be favoured over the metallic state, at least for the half-filled band case ( $\sum_{i,\sigma} n_{i\sigma} = N_{\text{el}} = N$ ) and at zero temperature. Strictly speaking, this holds in the adiabatic limit ( $\omega_0 = 0$ ) for ‘ $U$ -only’ (Hubbard model) and ‘ $\lambda$ -only’ (Peierls model) parameters. For the more general Holstein–Hubbard model, the situation is much less obvious. Clearly a large phonon frequency will act against any static ordering. If insulating phases exist nevertheless, their ground-state properties will depend on  $\omega_0$  and on the ratio of Coulomb and EP interactions  $u/\lambda$ . Likewise, the nature of the physical excitations is puzzling as well. While one expects ‘normal’ electron–hole excitations in the PI phase ( $U = 0$ ), charge (spin) excitations are known to be massive (gapless) in the MI state of the Hubbard model ( $\lambda = 0$ ). Thus, varying the

<sup>1</sup> The Holstein model [11] has been studied extensively as a paradigmatic model for polaron formation in the low-density limit. For commensurate band fillings, the coupling to the lattice supports charge ordering.

<sup>2</sup> The Hubbard model [12], originally designed to describe ferromagnetism of transition metals, has more recently been used as the probably most simple model to account for strong Coulomb correlation effects in the context of high-temperature superconductivity.

control parameter  $u/\lambda$ , a cross-over from standard quasi-particle behaviour to spin-charge separation might be observed in the more general 1D Holstein–Hubbard model.

The aim of this contribution is to affirm this physical picture and the anticipated phase diagram of the 1D Holstein–Hubbard model. For these purposes we adapt Lanczos exact diagonalisation (ED) [13], kernel polynomial (KPM) [14] and density-matrix renormalisation group (DMRG) [15] methods for EP problems (for an overview see [16, 17]). These numerical techniques allow us to obtain unbiased results for all interaction strengths with the full quantum dynamics of phonons taken into account.

## 1.2 Luttinger–Peierls Metal–Insulator Transition

To study the metal–insulator transition in 1D EP systems, we neglect, in a first step, the spin degrees of freedom in (1.1). Even so, the resulting 1D spinless fermion Holstein model,

$$H = -t \sum_{\langle i,j \rangle} c_i^\dagger c_j - g\omega_0 \sum_i (b_i^\dagger + b_i)n_i + \omega_0 \sum_i b_i^\dagger b_i, \quad (1.3)$$

is, despite its seeming simplicity, not exactly solvable. It is generally accepted, however, that the model exhibits a QPT from a metallic to an insulating phase at half-filling ( $N_e = N/2$ ) [18, 19]. During the last two decades, a wide range of analytical and numerical methods have been applied to map out the ground-state phase diagram in the whole  $g-\omega_0$  plane [18, 20–26], with significant differences, especially in the low-frequency intermediate EP coupling regime. In the adiabatic limit ( $\omega_0 \rightarrow 0$ ), the critical coupling  $\lambda_c(\omega_0)$  vanishes. In the anti-adiabatic ( $\omega_0 \rightarrow \infty$ ) strong EP coupling regime, the model can be transformed to the exactly solvable XXZ model [18, 23], which shows a transition of Kosterlitz–Thouless type.

Before we determine the metal–insulator phase boundary, let us characterise the metallic and insulating phases themselves. According to Haldane’s Luttinger liquid (LL) conjecture [27], an 1D gapless (metallic) system of interacting fermions should belong to the Tomonaga–Luttinger universality class [28, 29]. As the Holstein model of spinless fermions is expected to be gapless at weak couplings  $g$ , the system is described by (non-universal) LL parameters  $u_\rho$  (charge velocity) and  $K_\rho$  (correlation exponent).

In the following, we try to determine  $u_\rho$  and  $K_\rho$  by large-scale DMRG calculations. To leading order, the charge velocity and the correlation exponent is related to the ground-state energy of a finite system with  $N$  sites

$$\frac{E_0(N)}{N} = \varepsilon_0(\infty) - \frac{\pi}{3} \frac{u_\rho}{2} \frac{1}{N^2} \quad (1.4)$$

( $\varepsilon_0(\infty)$  denotes the bulk ground-state energy density) and the charge excitation gap

$$\Delta_c(N) = E_0^\pm(N) - E_0(N) = \pi \frac{u_\rho}{2} \frac{1}{K_\rho} \frac{1}{N} \quad (1.5)$$

(here  $E_0^\pm(N)$  is the ground-state energy with  $\pm 1$  fermion away from half-filling  $n = N_{\text{el}}/N = 0.5$ ). Note that the LL scaling relations (1.4) and (1.5) were derived for the pure electronic spinless fermion model only [30]. A careful finite-size analysis shows, however, that they also hold for the case that a finite EP is included [31]. Figure 1.2 shows the resulting LL parameters, exemplarily for two frequencies belonging to the adiabatic (upper left panel) and anti-adiabatic (upper right panel) regimes. Interestingly, the LL phase splits into two different regions: for small phonon frequencies, the effective fermion–fermion interaction is attractive ( $K_\rho > 0$ ), while it is repulsive ( $K_\rho < 0$ ) for large frequencies. In the latter region, the kinetic energy ( $\propto u_\rho$ ) is strongly reduced and the charge carriers behave like (small) polarons. In between, there is a transition line  $K_\rho = 1$ , where the LL is made up of (almost) non-interacting particles. The LL scaling breaks down just at a critical coupling  $g_c(\omega_0/t)$ , signalling the transition to the CDW (charge density wave) state. We find, for example  $g_c^2(\omega_0/t = 0.1) \simeq 7.84$  and  $g_c^2(\omega_0/t = 10) \simeq 4.41$ .

The middle panels of Fig. 1.2 prove the existence of CDW long-range order above  $g_c$ . Here the staggered charge structure factor

$$S_c(\pi) = \frac{1}{N^2} \sum_{i,j} (-1)^j \langle (n_i - n)(n_{i+j} - n) \rangle \quad (1.6)$$

unambiguously scales to a finite value in the thermodynamic limit ( $N \rightarrow \infty$ ). Simultaneously,  $\Delta_c(\infty)$  acquires a finite value. In contrast, we have  $S_c(\pi) \rightarrow 0$  in the metallic regime ( $g < g_c$ ). Note that such a finite-size scaling, including dynamical phonons, is definitely out of range for any ED calculation. The CDW at strong EP coupling is connected to a Peierls distortion of the lattice and can be classified as traditional band insulator and polaronic superlattice in the strong-coupling adiabatic and anti-adiabatic regimes, respectively.

The optical absorption spectra shown in the lower panels of Fig. 1.2 elucidate the different nature of the CDW for small and large adiabaticity ratios in more detail. The regular part of the optical conductivity,<sup>3</sup>

$$\sigma^{\text{reg}}(\omega) = \sum_{m>0} \frac{|\langle \psi_0 | \hat{j} | \psi_m \rangle|^2}{E_m - E_0} \delta[\omega - (E_m - E_0)], \quad (1.7)$$

takes into account finite-frequency transitions from the ground state  $|\psi_0\rangle$  to excited quasi-particle states  $|\psi_m\rangle$  in the same particle sector.<sup>4</sup> Importantly, the current operator  $\hat{j} = it \sum_i (c_i^\dagger c_{i+1} - c_{i+1}^\dagger c_i)$  has finite matrix elements between

<sup>3</sup> The evaluation of dynamical correlation functions like  $\sigma^{\text{reg}}(\omega)$  can be carried out by means of the very efficient and numerically stable ED-KPM algorithm [14].

<sup>4</sup> In (1.7),  $\sigma^{\text{reg}}(\omega)$  is given in units of  $\pi e^2$  and we have omitted an  $1/N$  prefactor.

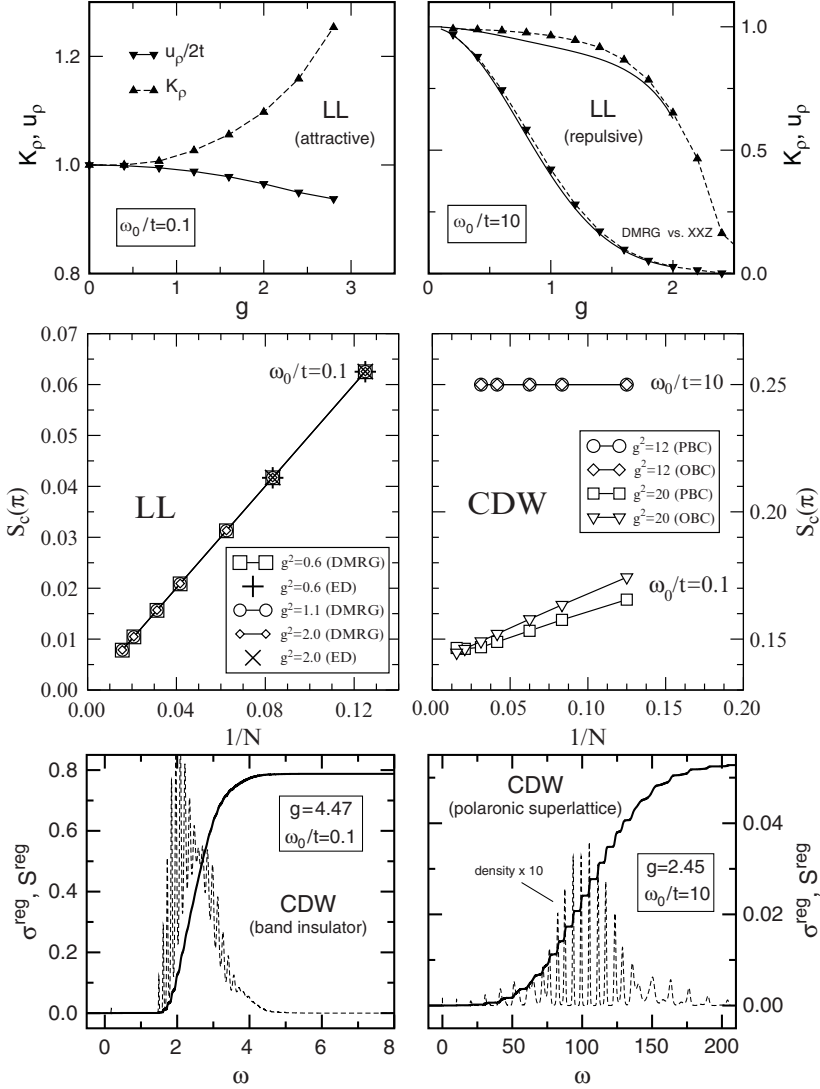


**Fig. 1.2.** Basic properties of the 1D half-filled spinless fermion Holstein model: Luttinger liquid parameters  $u_p$  and  $K_p$  in the metallic region (*top panels*; the *solid lines* in the right panel gives the asymptotic results for the XXZ model), finite-size scaling of the charge structure factor  $S_c(\pi)$  below and above the metal–insulator transition (*middle panels*), and optical response  $\sigma^{\text{reg}}(\omega)$  in the CDW regime (*lower panels*). See text for further explanation

states of different site-parity only. In the adiabatic region, the most striking feature is the sharp absorption threshold and large spectral weight contained in the incoherent part of optical conductivity. In the anti-adiabatic regime,

the CDW is basically a state of alternate self-trapped polarons, which means that the electrons are heavily dressed by phonons. As the renormalised band dispersion is extremely narrow, finite-size gaps are reduced as well. Therefore,  $\Delta_{\text{opt}}$  read off from Fig. 1.2 yields the correct CDW gap.

Further information can be obtained from single-particle excitation spectra. The  $T = 0$  electron spectral function is related to the one-electron Green function via

$$A(k, \omega) = -\frac{1}{\pi} \text{Im} G(k, \omega) = A^+(k, \omega) + A^-(k, \omega), \quad (1.8)$$

where

$$A^\pm(k, \omega) = -\frac{1}{\pi} \text{Im} \lim_{\eta \rightarrow 0^+} \left\langle \psi_0 | c_k^\mp \frac{1}{\omega + i\eta \mp H} c_k^\pm | \psi_0 \right\rangle, \quad (1.9)$$

with  $c_k^- = c_k$ ,  $c_k^+ = c_k^\dagger$ .  $A^-(k, \omega)$  [ $A^+(k, \omega)$ ] describes [inverse] photoemission of an [injected] electron with momentum  $k$  and energy  $\omega$ . The spectral functions shown in Fig. 1.3 have been calculated by an elaborate dynamical DMRG method [32, 33]. As we are in the insulating CDW phase, we observe a single-particle excitation gap at the Fermi momenta  $k_F = \pm\pi/2$ . Below and above the gap, the spectrum shows broad multi-phonon absorption bands

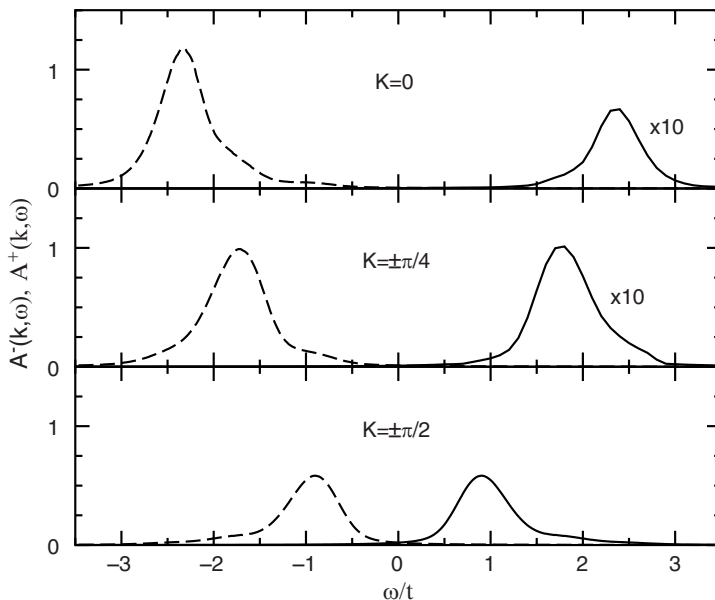


**Fig. 1.3.** Spectral functions  $A^-(k, \omega)$  (for electron removal,  $\omega < 0$ ) and  $A^+(k, \omega)$  (for electron injection  $\omega > 0$ ) for the spinless Holstein model at half-filling ( $N = 10$  with periodic boundary conditions (PBC)). The system is in the CDW (Peierls insulating) phase ( $g = 4$ ,  $\omega_0/t = 0.1$ ). Note that only  $|k| \leq \pi/2$  is shown because  $A(k \pm \pi, \omega) = A(k, -\omega)$

whose maxima roughly follow a renormalised cosine tight-binding dispersion in momentum space.

The  $T = 0$  phonon spectral function is defined as

$$B(q, \omega) = -\frac{1}{\pi} \text{Im} D(q, \omega), \quad (1.10)$$

with

$$D(q, \omega) = \lim_{\eta \rightarrow 0^+} \left\langle \psi_0 | \hat{x}_q \frac{1}{\omega + i\eta - H} \hat{x}_{-q} | \psi_0 \right\rangle \quad (1.11)$$

for  $\omega \geq 0$  and  $\hat{x}_q = N^{-1/2} \sum_j \hat{x}_j e^{-i(jq)}$ . For the spinless fermion Holstein model (1.3),  $B(q, \omega)$  is symmetric in  $q$ , and we have a dispersionsless bare propagator  $D_0(q, \omega) = 2\omega_0/(\omega^2 - \omega_0^2)$ . EP interaction will renormalise the phonon frequency, whereby  $D(q, \omega)$  attains a  $q$ -dependence. To determine the  $q$ -dependence of  $B(q, \omega)$  for the infinite lattice, we exploit ED in combination with cluster perturbation theory [26, 34]. The density plots shown in Fig. 1.4

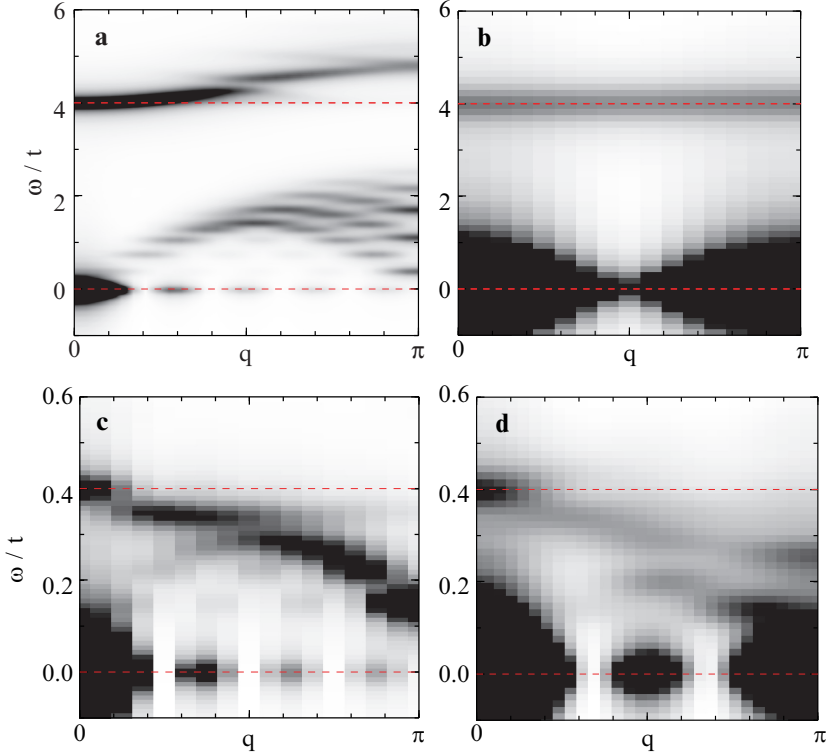


**Fig. 1.4.** Density plots of the CPT phonon spectral function  $B(q, \omega)$ , where panels (a)–(d) correspond to the repulsive LL ( $\omega_0/t = 4$ ,  $g^2 = 0.5$ ), polaron superlattice ( $\omega_0/t = 4$ ,  $g^2 = 5$ ), attractive LL ( $\omega_0/t = 0.4$ ,  $g^2 = 2.5$ ), and band insulator ( $\omega_0/t = 0.4$ ,  $g^2 = 5$ ) regimes, respectively (taken from [26])

summarise the differences between the anti-adiabatic and adiabatic regimes, and between the LL and CDW phases of the spinless fermion Holstein model. In the anti-adiabatic case, we observe two phonon signatures for all  $g > 0$ . In the LL phase, the bare phonon mode hardens, whereas a second mode becomes strongly over-damped near  $q = \pi$  [panel (a)]. Panel (b) reveals a dispersionsless signal at  $\omega = \omega_0$ , as well as the flat polaron band at  $\omega \approx 0$  for the polaronic CDW state. Quite differently, in the adiabatic case [panel (c)], we see that renormalised phonon dispersion  $\omega(q)$  softens with increasing EP coupling, leading to a degeneracy of excitations with  $q = 0, \pi$  at  $g_c$ . Above the Peierls transition we find – in agreement with recent Monte Carlo simulations [35] – that the soft  $q = \pi$  phonon mode splits into two branches with the upper one hardening as the EP coupling increases further [panel (d)].<sup>5</sup> Thus, with increasing phonon frequency, we find a cross-over from a soft-mode (displacive) to a central-peak-like (order-disorder-type) phase transition, similar to the analysis of the spin–Peierls transition motivated by  $\text{CuGeO}_3$  [21] (cf. Sect. 5.1).

Finally the phase diagram of the 1D Holstein model is presented in Fig. 1.5. The regions where the system typifies as repulsive LL, attractive LL, polaronic superlattice, or band insulator are indicated. While we observe a rather smooth cross-over between different states within the metallic respectively in-

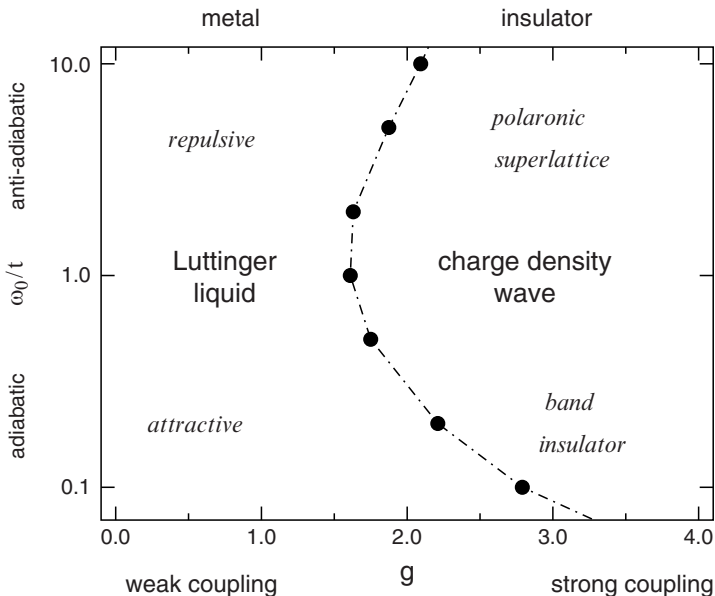


**Fig. 1.5.** Ground-state phase diagram of the 1D half-filled Holstein model of spinless fermions obtained by DMRG

<sup>5</sup> The strong zero-energy absorption feature at  $\pi/2$  is an artifact of the small cluster size and the open boundary conditions used in the ED-CPT scheme.

solulating ‘domains’, there is a true metal–insulator QPT between the LL and the CDW phase. Three different methods were used to determine the phase boundary. First we employ an optimised phonon diagonalisation method [24] and look for an upturn of the charge structure factor in passing from LL to CDW. The second DMRG-based method was inspired by work on the frustrated Heisenberg model and exploits a level crossing criteria between the charge gap and the ‘one-photon’ excitation gap [23]. The third method rests on a DMRG finite-size scaling of the charge structure factor (cf. Fig. 1.2). The results basically agree and above all confirm that a finite critical EP coupling is required to set up the CDW phase provided  $\omega_0 > 0$ .

### 1.3 Peierls–Mott Insulator–Insulator Transition

Now we include the spin degrees of freedom and ask for the effect of a finite Coulomb interaction. The ground state of the pure Holstein model ( $U = 0$ ) is a Peierls distorted state with staggered charge order for  $g > g_c(\omega_0)$  [36,37], that is as in the Holstein model of spinless fermions, quantum phonon fluctuations destroy the Peierls state for  $g < g_c$ .

The charge structure factor,  $S_c(\pi)$  [cf. (1.6)], and spin structure factor,

$$S_s(\pi) = \frac{1}{N^2} \sum_{i,j} (-1)^j \langle S_i^z S_{i+j}^z \rangle \quad \text{with} \quad S_i^z = \frac{1}{2}(n_{i\uparrow} - n_{i\downarrow}), \quad (1.12)$$

shown in Fig. 1.6 for the full Holstein–Hubbard model, indicate pronounced CDW and weak SDW (spin density wave) correlations, provided  $u/\lambda < 1$ . Increasing the Hubbard interaction  $u$  at fixed EP coupling  $\lambda$  and frequency  $\omega_0$ , the CDW correlations become strongly suppressed, whereas the spin structure factor at  $q = \pi$  is enhanced. To conclude about a possible existence of charge and/or spin long-range order, one has to determine  $S_c(\pi)$  and  $S_s(\pi)$  for different system sizes, followed by a finite-size scaling of the data. The size-dependence of the DMRG results for  $S_{c/s}(\pi)$  is shown in the lower panels of Fig. 1.6. In the PI phase,  $S_c(\pi)$  is almost constant and scales to a finite value, indicating true CDW long-range order, whereas  $S_s(\pi)$  obviously scales to zero as  $N \rightarrow \infty$ . By contrast, in the MI regime, our data provides strong evidence for vanishing charge and also spin order in the thermodynamic limit. Consequently, the PI exhibits CDW order, that is alternating empty and doubly occupied sites, while the MI is characterised by short-ranged anti-ferromagnetic spin correlations (see Fig. 1.7).<sup>6</sup>

Figure 1.8 displays the (inverse) photoemission spectra for the Holstein–Hubbard model, where

$$A_\sigma^\pm(k, \omega) = \sum_m |\langle \psi_m^\pm | c_{k\sigma}^\pm | \psi_0 \rangle|^2 \delta[\omega \mp (E_m^\pm - E_0)], \quad (1.13)$$

<sup>6</sup> Here the staggered spin–spin correlations decay algebraically at large distances.

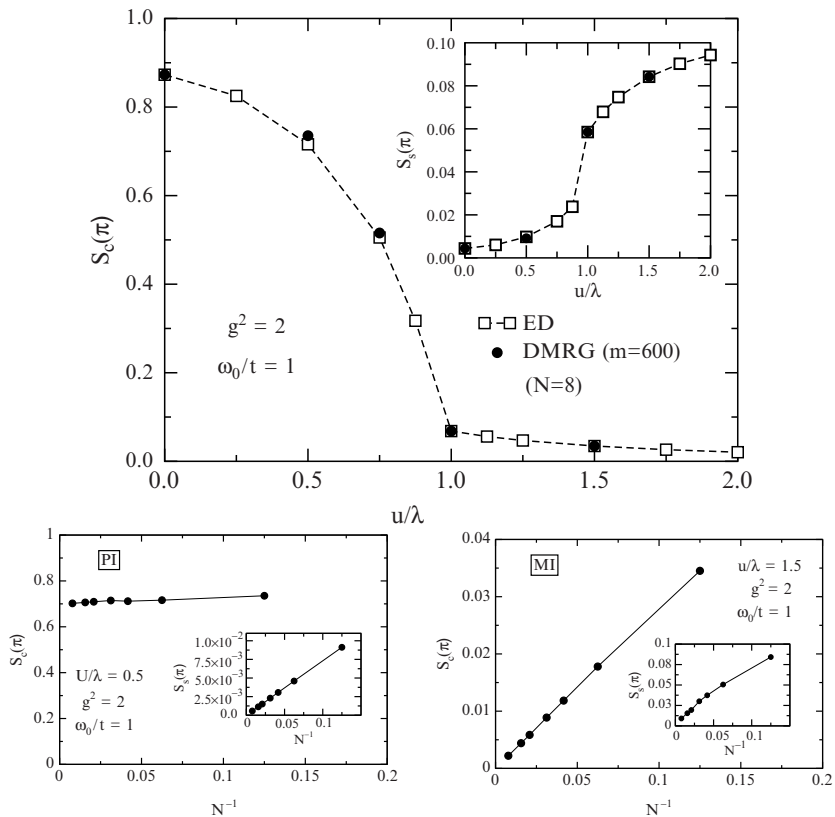


**Fig. 1.6.** Staggered charge and spin structure factors in the half-filled 1D Holstein-Hubbard model (1.1). The *upper panel* compares ED (*squares*) and DMRG (*filled circles*) results for a small eight-site system (PBC) with  $\lambda = 1$ ,  $\omega_0/t = 1$ . The *lower panels* show the finite-size scaling of  $S_c(\pi)$  and  $S_s(\pi)$  (inset) in the PI (*left panel*) and MI (*right panel*) regimes

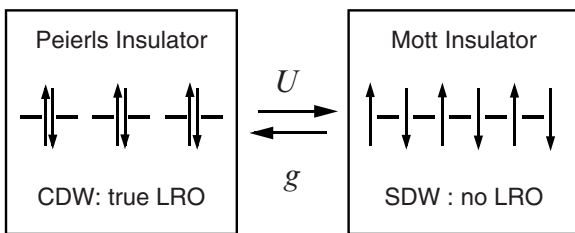


**Fig. 1.7.** Schematic structure of Peierls and Mott insulating states

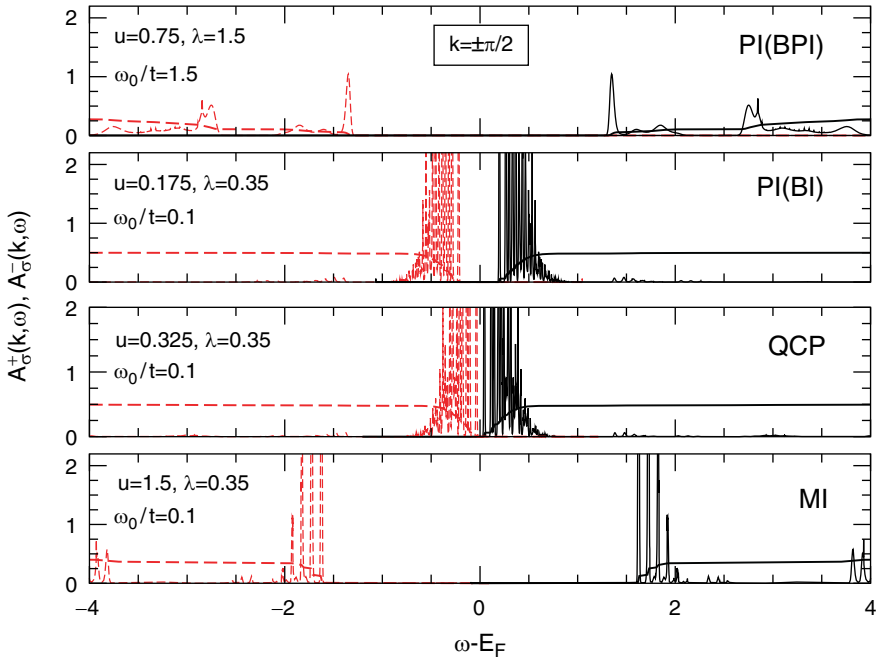


**Fig. 1.8.** Spectral densities for photoemission ( $A_{\sigma}^{-}(k, \omega)$ ; *dashed lines*) and inverse photoemission ( $A_{\sigma}^{+}(k, \omega)$ ; *solid lines*) in the  $k = \pm\pi/2$  sector of the half-filled Holstein-Hubbard model. Data were obtained by applying our ED-KPM scheme. Shown are typical results obtained for the case of a bipolaronic insulator (BPI), a Peierls band insulator (BI), a system near the PI-MI quantum critical point (QCP), and a Mott insulator (MI) (from *top to bottom*). The corresponding integrated densities  $S_{\sigma}^{\pm}(k, \omega) = \int_{\mp\infty}^{\omega} d\omega' A_{\sigma}^{\pm}(k, \omega')$  are also indicated

with  $c_{k\sigma}^{+} = c_{k\sigma}^{\dagger}$  and  $c_{k\sigma}^{-} = c_{k\sigma}$  [cf. (1.9)]. To monitor a band splitting induced by the Hubbard and Holstein couplings, we focus on the results at the Fermi momenta  $k_F = \pm\pi/2$  (PBC).<sup>7</sup>

The most prominent feature we observe in the PI regime is a finite gap at  $k = \pm\pi/2$ . At high phonon frequencies, the insulating behaviour is associated with localised bipolarons forming a CDW state (BPI, upper panel). Because of strong polaronic effects, an almost flat band dispersion with exponentially small (electronic) quasi-particle weight results [6]. The dominant peaks in the incoherent part of the (inverse) photoemission spectra are related to multiples of the (large) bare phonon frequency. The situation changes if the phonon frequency is small (adiabatic regime). Here, for the traditional BI, a rather broad photoemission signature appears. Within these excitation bands, the spectral weight is almost uniformly distributed, which is a clear indication of the multi-phonon absorption and emission processes that accompany every

<sup>7</sup> Spectra for the other allowed momenta of our eight-site system are given in [6].

single-particle excitation in the PI. The line shape reflects the Poisson-like distribution of the phonons in the ground state. Away from the Fermi momenta, the lower and upper bands closely follow a (slightly renormalised) cosine dispersion. If we enhance the Hubbard interaction at fixed EP coupling strength, the Peierls gap weakens and finally closes at about  $(u/\lambda)_c \simeq 1$ , which marks the PI-MI cross-over quantum critical point (QCP). This is the situation shown in the middle panel. Approaching the QCP, the ground state and the first excited state become degenerate. The QCP is characterised by gapless charge excitations at the Fermi momenta but perhaps should not be considered as metallic because the Drude weight in the case of a degenerate ground state is ill-defined [38]. If the Hubbard interaction further increases, Coulomb repulsion overcompensates the attractive on-site EP coupling and the single-particle excitation spectrum becomes gapped again (lowest panel). The Mott–Hubbard correlation gap almost coincides with the optical gap  $\Delta_{\text{opt}}$  determined by evaluating the regular part of the optical conductivity for the same parameters. The form of the MI spectra is quite different from PI case. Contrary to the PI phase in the MI regime, the lowest peak in each  $k$  sector is clearly the dominant one. The dispersion of the lower (upper) Hubbard band can be derived tracing the uppermost (lowest) excitations in each  $k$  sector. As  $N$  goes to infinity for  $u \gg 1$ , the lower Hubbard band will be completely filled, and consequently the system behaves as an insulator at  $T = 0$ .

The many-body charge and spin excitation gaps,

$$\Delta_c = E_0^+(1/2) + E_0^-(-1/2) - 2E_0(0) \quad (1.14)$$

$$\Delta_s = E_0(1) - E_0(0), \quad (1.15)$$

can also be used to characterise the different phases of the Holstein–Hubbard model. Here  $E_0^{(\pm)}(S^z)$  is the ground-state energy at half-filling (with  $N_e = N \pm 1$  particles in the sector with total spin- $z$  component  $S^z$ ). As we compare ground-state energies calculating the charge and spin gaps, lattice relaxation effects arising from different particle numbers are included. This is of course not the case when determining the single-particle functions (1.9) or (1.13). Obviously, the DMRG finite-size scaling presented in Fig. 1.9 for  $\Delta_{c/s}$  substantiates our introductory discussion.  $\Delta_c$  and  $\Delta_s$  are finite in the PI and will converge further as  $N \rightarrow \infty$ . Compared to the BI phase, the finite-size dependence of  $\Delta_c$  and  $\Delta_s$  is much weaker in the BPI phase because the small bipolarons that emerge are rather localised objects. Both gaps seem to vanish at the quantum phase transition point of the Holstein–Hubbard model with finite-frequency phonons, but in the critical region the finite-size scaling is extremely delicate. In the MI we found a finite charge excitation gap, which in the limit  $u/\lambda \gg 1$  scales to the optical gap of the Hubbard model, whereas the extrapolated spin gap remains zero. This can be taken as a clear indication for spin-charge separation.

So far we can summarise our findings by the schematic ground-state phase diagram shown in Fig. 1.10.

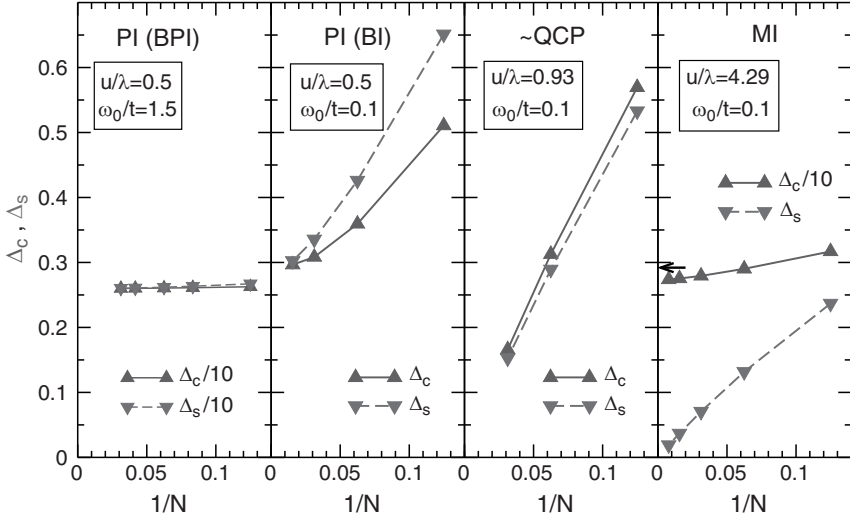


**Fig. 1.9.** DMRG finite-size scaling of spin- and charge-excitation gaps in the HHM at  $\lambda = 0.35$  and  $\omega_0/t = 0.1$ , where open boundary conditions were used. The accessible system sizes are smaller at larger  $\lambda/u$ , where an increasing number of (phononic) pseudo-sites is required to reach convergence with respect to the phonons. The arrow marks the value of the optical gap  $\Delta_{\text{opt}}$  for the Bethe ansatz solvable 1D Hubbard model, which is given by  $\Delta_{\text{opt}}/4t = u - 1 + \ln(2)/2u$  in the limit of large  $u > 1$  [39]

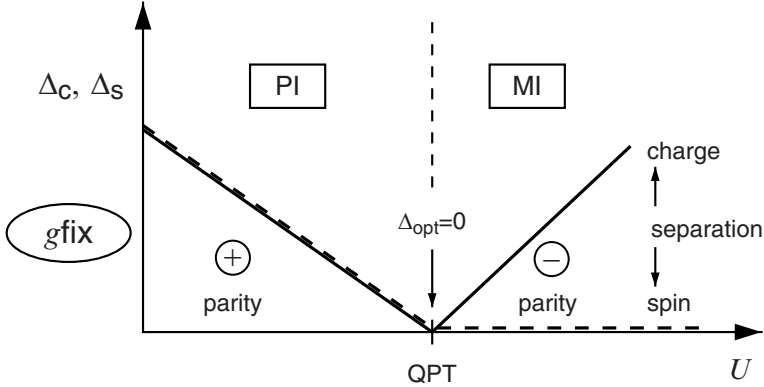


**Fig. 1.10.** PI-MI QPT in the strong coupling regime of the Holstein-Hubbard model. For finite periodic chains with  $N = 4n$ , the MI-PI quantum phase transition could be identified by a ground-state level crossing associated with a change in the parity eigenvalue  $P = \pm$  [40], where the site inversion symmetry operator  $P$  is defined by  $Pc_{i\sigma}^\dagger P^\dagger = c_{N-i\sigma}^\dagger$  [41].

## 1.4 On the Possibility of an Intervening Metallic Phase

Recently there has been some speculation that, despite the electron–electron and EP interactions each separately favouring insulating phases, together they can mediate an unexpected intermediate metallic state [5, 9]. Applying a variable-displacement Lang–Firsov scheme, a rather intriguing behaviour in the local magnetic moment and the renormalised hopping integral was found in the CDW–SDW cross-over region and traced back to the appearance of a metallic phase in the weak-coupling regime [5]. The intermediate phase has been confirmed by a numerical study based on stochastic series expansion quantum Monte Carlo with directed loops [9], where the slope of the finite-size scaled charge and spin structure factors in the long-wavelength limit was evaluated:

$$K_{\rho/\sigma} = \lim_{q \rightarrow 0} \frac{1}{\pi q} \frac{1}{N} \sum_{j,k} e^{iq(j-k)} \langle (n_{j,\uparrow} \pm n_{j,\downarrow})(n_{k,\uparrow} \pm n_{k,\downarrow}) \rangle.$$

$K_{\rho/\sigma}$  are the LL charge/spin correlation exponents.  $K_{\rho}$  values greater than 1 were taken as indication for dominant attractive superconducting correlations (SC). The resulting ground-state phase diagram shows two different sequences of phases as  $\lambda$  increases, either Mott–Peierls in the strong-coupling region of large  $u$  (as in discussed in Sect. 3) or Mott–SC–Peierls in the weak-coupling region of small  $u$  (see Fig. 1.11, upper column). At smaller phonon frequencies  $\omega_0$ , the SC region shrinks. As it is numerically difficult to determine the phase boundaries by exploiting the local magnetic moment, the effective hopping integral or  $K_{\rho/\sigma}$ , we re-investigated the weak-coupling Holstein–Hubbard model by calculating the charge and spin gaps, defined in (1.14) and (1.15), respectively, as well as the two-particle excitation gap [42]

$$\Delta_{c_2} = E_0^{2+}(0) + E_0^{2-}(0) - 2E_0(0). \quad (1.16)$$

This gap corresponds to the charge gap in a bipolaronic insulator and is an upper limit for it in any other phase. Let us denote the (single-particle) charge gap (1.14) by  $\Delta_{c_1}$  in this section. Then, of course, one- and two-particle excitation gaps should simultaneously open if we enter the PI and MI phases. If the PI phase is a bipolaronic insulator (superlattice) rather than a traditional Peierls band insulator, mobile bipolarons may occur first in the dissolving process of the PI, as the  $\lambda/u$  ratio is lowered. Such a bipolaronic metal/liquid phase will then be characterised by  $\Delta_{c_2} = 0$  but finite  $\Delta_{c_1}$  (and  $\Delta_s$ ). Adding/removing a single particle from the metallic bipolaron phase is energetically costly because the bipolarons are (tightly) bound. A bipolaron as a whole, however, can be added or removed without effort.

The left lower panel of Fig. 1.11 demonstrates that this scenario holds in the anti-adiabatic ( $\omega_0/t = 5$ ) weak-coupling regime. As the EP coupling gets weaker, we enter a region where  $\Delta_{c_1} > 0$  but  $\Delta_{c_2} \rightarrow 0$  (see, e.g. the data for  $\lambda = 0.625$ ).  $\Delta_{c_2}$  stays zero as  $\Delta_{c_1}$  vanishes at still smaller  $\lambda$  ( $u$  fixed),

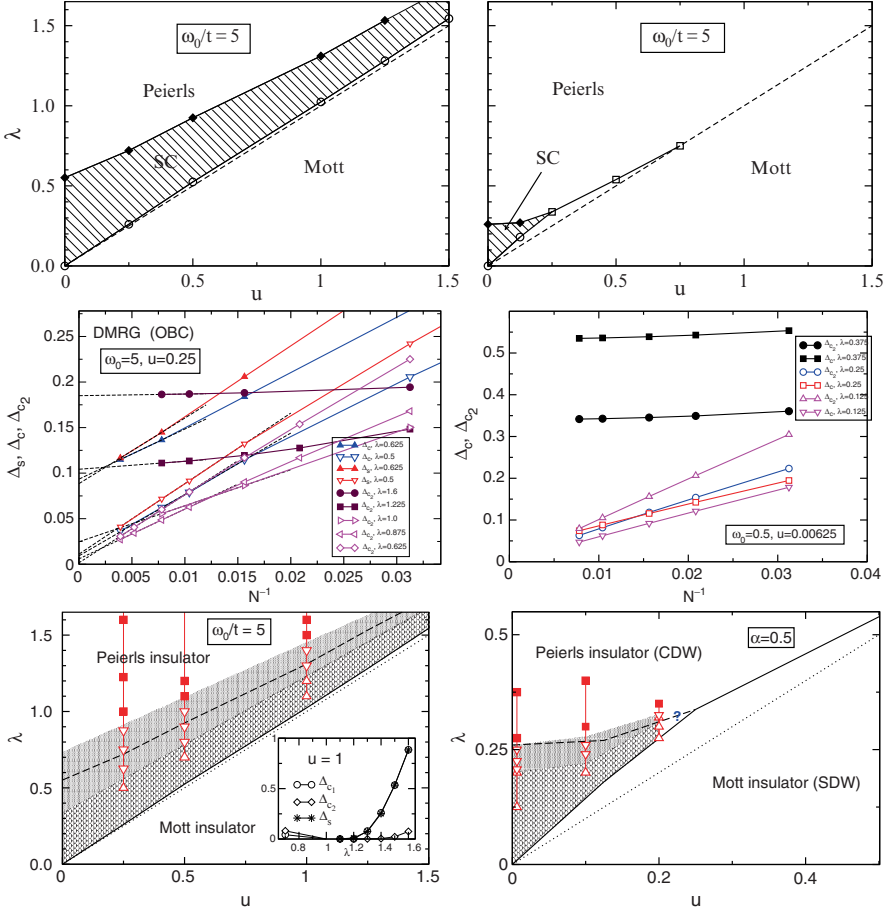


**Fig. 1.11.** Phase diagram of the Holstein–Hubbard model for weak couplings. The *left (right)* panels belong to the anti-adiabatic (adiabatic) regime. The *upper panels* are redrawn from Fig. 4 of [9], where the *shaded areas* show the extension of the intermediate metallic phase as determined from the behaviour of  $K_{\rho/\sigma}$ . The middle column panels display the finite-size scaling of spin, single-particle and two-particle excitation gaps. The lower column shows the phase diagram obtained from our DMRG calculation [42]. Here *filled squares*, *open triangles down*, and *open triangles up*, denote the PI, bipolaronic metal and Luttinger-liquid metal phases, respectively. The *inset* in the lower left panel gives the  $(N \rightarrow \infty)$  extrapolated values of the one-particle, two-particle and spin excitation gaps at  $u = 1$ . Note that  $\Delta_{c_2}$  is twice as large as  $\Delta_{c_1}$  in the MI phase. For further explanation see text

until we enter the MI state. We note that the PI-metal phase boundary is shifted compared to the results of [9], while the metal-MI transition line is the very same. That is, taking  $\Delta_{c_2} = 0$  as a criterion for the instability of the PI phase, we find an even larger region for the PI-MI intervening state. Second,

within the metallic state, our data indeed suggests a cross-over between a bipolaronic liquid ( $\Delta_{c_2} = 0$ ;  $\Delta_{c_1}, \Delta_s > 0$ ) and a Luttinger liquid ( $\Delta_{c_2} = \Delta_{c_1} = \Delta_s = 0$ ). The corresponding results for the adiabatic regime ( $\omega_0/t = 0.5$ ) are given in right lower panel of Fig. 1.11. Again we have strong evidence for an intermediate metallic state. The region where bound mobile charge carriers (bipolarons) exist, however, now is a small strip between the PI and metal phases only, and expected to vanish if the adiabaticity ratio  $\omega_0/t$  goes to zero.

## 1.5 Limiting Cases

### 1.5.1 Adiabatic Holstein–Hubbard Model

In the adiabatic limit  $\omega_0 = 0$ , the general Holstein–Hubbard Hamiltonian (1.1) reduces to

$$H = H_{t-U} - \sum_{i,\sigma} \Delta_i n_{i\sigma} + \frac{\kappa}{2} \sum_i \Delta_i^2, \quad (1.17)$$

where  $H_{t-U}$  constitutes the conventional Hubbard Hamiltonian. In addition, the adiabatic Holstein–Hubbard model (1.17) includes the elastic energy of the lattice with ‘spring constant’  $\kappa$ . Within this so-called ‘frozen phonon’ approach,  $\Delta_i = (-1)^i \Delta$  is a measure of the static, staggered density modulations of the PI phase. For the adiabatic Holstein–Hubbard model a discontinuous PI–MI transition is easily verified in the atomic limit  $t = 0$ , where  $\Delta = 1/\kappa$  for  $U < U_c = 1/\kappa$  and  $\Delta = 0$  for  $U > U_c$ . The first-order nature persists for finite small  $t$ , that is in the strong coupling regime  $U$ ,  $\kappa^{-1} \gg t$ . However, we have demonstrated by an ED study that the transition is second order in the weak coupling regime  $U$ ,  $\kappa^{-1} \ll t$  [37]. This implies a continuous decrease of  $\Delta(U)$ .

We summarise our previous findings in the phase diagram shown in Fig. 1.12. In the Peierls BI phase for  $U < U_{\text{opt}}$ , the spin and charge excitation gaps are equal and finite, and remarkably  $\Delta_{\text{opt}} \neq \Delta_c$ . Here  $U_{\text{opt}}$  marks the point when the site-parity sectors become degenerate and the optical absorption gap  $\Delta_{\text{opt}}$  disappears. At  $U = U_{\text{opt}}$ ,  $\Delta_{\text{opt}} = 0$  but  $\Delta_c = \Delta_s > 0$ . For  $U \geq U_s$ , the usual MI phase with  $\Delta_{\text{opt}} = \Delta_c > \Delta_s = 0$  is realised. For strong coupling  $U_{\text{opt}} = U_s$  holds. In weak coupling there exists an intermediate region  $U_{\text{opt}} < U < U_s$  in which all excitation gaps are finite. The CDW persists for all  $U < U_s$ . The site-parity eigenvalue is  $P = +1$  in the PI and  $P = -1$  in the MI phase. It is natural to expect an additional ordering phenomenon in the window  $U_{\text{opt}} < U < U_s$ . Here a bond order wave (BOW) with a finite expectation value of the staggered bond charge  $B = \frac{1}{N} \sum_{i\sigma} (-1)^i \langle c_{i\sigma}^\dagger c_{i+1\sigma} + \text{H.c.} \rangle$  is the natural candidate.

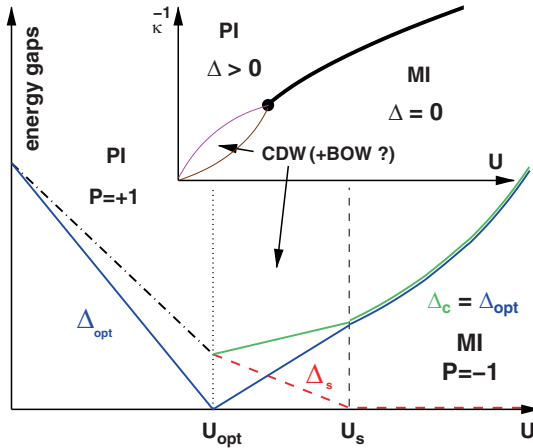


**Fig. 1.12.** Qualitative phase diagram of the adiabatic Holstein–Hubbard model. *Inset:* Transition scenario in the weak coupling regime  $U, \kappa^{-1} \ll t$ , where the PI-MI transition therefore evolves across two critical points



**Fig. 1.13.** Structure of the Mott SDW and spin–Peierls phases

### 1.5.2 Spin–Peierls Model

In the preceding sections we have seen that the interaction of electronic and vibrational degrees of freedom can lead to an instability of 1D metals towards lattice distortion. A similar effect is observed in quantum spin chains (which implement, in some sense, the  $t = 0$  large  $U$  limit of the half-filled Hubbard model), where the coupling to the lattice can cause a so-called spin–Peierls transition from a spin liquid with gapless excitations to a dimerised phase with an excitation gap (see Fig. 1.13). Experimentally such behaviour was first observed in the 1970s for organic compounds of the TTF and TCNQ family [43]. The topic regained attention after the discovery of the first inorganic spin–Peierls compound  $\text{CuGeO}_3$  in 1993 [44]. The most significant feature distinguishing this material from other spin–Peierls compounds is the high frequency  $\omega_0$  of the involved optical phonons, which is comparable to the magnetic exchange interaction  $J$ .

As an archetypal model for this type of spin–Peierls system we consider the anti-ferromagnetic Heisenberg chain coupled to optical phonons

$$H = J \sum_i \mathbf{S}_i \mathbf{S}_{i+1} + \omega_0 \sum_i b_i^\dagger b_i + H_{sp}, \quad (1.18)$$

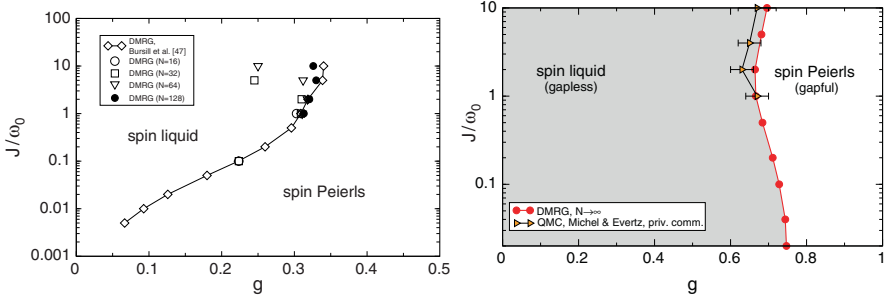


**Fig. 1.14.** Ground-state phase diagram of the spin–Peierls chain with difference (*left panel*) and local coupling (*right panel*)

where  $\mathbf{S}_i$  denote spin- $\frac{1}{2}$  operators at lattice site  $i$ . For the spin–phonon interaction one usually considers two simple forms

$$H_{\text{sp}}^d = g\omega_0 \sum_i (b_i^\dagger + b_i)(\mathbf{S}_i \mathbf{S}_{i+1} - \mathbf{S}_{i-1} \mathbf{S}_i), \quad (1.19)$$

$$H_{\text{sp}}^l = g\omega_0 \sum_i (b_i^\dagger + b_i) \mathbf{S}_i \mathbf{S}_{i+1}. \quad (1.20)$$

$H$  with the first (difference) type of spin–phonon interaction (1.19) has been studied with a large number of methods, including perturbation theory [45,46], flow equations [47], ED [46] and DMRG [48,49]. The latter approach identified the ground-state phase diagram displayed in Fig.1.14 (left panel). All these studies agree on the main finding that at  $\omega_0 > 0$  the system undergoes a QPT only for some finite value of  $g$ . The nature of the QPT from the gapless to the dimerised phase is rather well understood: For finite phonon frequency  $\omega_0$  the spin–phonon coupling  $g$  leads to effective spin interactions beyond nearest-neighbour exchange, that is the low energy physics is governed by a frustrated Heisenberg model, which has a gapped ground-state at sufficiently large frustration [50].

For the second (local) type of spin–phonon coupling (1.20), which applies to  $\text{CuGeO}_3$ , the precise location of the phase boundary has been determined only quite recently by a high-performance, parallel version of the well-known two-block finite-lattice DMRG algorithm [51] (see Fig.1.14, right panel). To detect the quantum phase transition from the gapless to the dimerised phase, we used the established criterion of level-crossing between the first singlet and the first triplet excitation.

## 1.6 Conclusions

In summary, we have addressed the metal–insulator and insulator–insulator transition problem in 1D strongly coupled electron–phonon systems. The generic features observed are relevant to several classes of low-dimensional

materials. Applying numerical diagonalisation methods based on Lanczos, density matrix renormalisation group and kernel polynomial algorithms, we analysed the general Holstein–Hubbard model at half-filling and obtained, by the use of present-day leading-edge supercomputers, basically exact results for both ground-state and spectral properties in the overall region of electron–electron/electron–phonon coupling strengths and phonon frequencies.

For the spinless Holstein model we found that for weak electron–phonon couplings the system resides in a metallic (gapless) phase described by two non-universal Luttinger-liquid parameters. Increasing the electron-phonon coupling, a quantum phase transition to a Peierls insulating state takes place, which is accompanied by drastic changes in the optical response of the system.

Of a similar type is a Heisenberg spin chain coupled to optical phonons, which for increasing spin-lattice coupling undergoes a quantum phase transition from a gapless spin liquid to a gapped phase with lattice dimerisation.

For the more involved Holstein–Hubbard model, with respect to the metal, the electron–electron interaction favours a Mott insulating state, while the electron–phonon coupling is responsible for the Peierls insulator to occur. True long-range (charge density wave) order is established in the Peierls insulator phase only. The Peierls insulator typifies a band insulator in the adiabatic weak-to-intermediate coupling range or a bipolaronic insulator for non-too-anti-adiabatic strong-coupling. The optical conductivity signals that the quantum phase transition between the Mott and Peierls insulator phases is connected to a change in the ground-state site-parity eigenvalue (of finite systems with PBC). While we found only one critical point separating Peierls and Mott insulating phases in the strong-coupling regime, there is strong evidence for an intervening metallic state in the weak-coupling regime. This is in accordance with results obtained in the adiabatic limit ( $\omega_0 = 0$ ), where two successive transitions have been detected for weak couplings as well. The Peierls-to-Mott transition scenario is corroborated by the behaviour of the spin- and charge excitation gaps. From a DMRG finite-size scaling, we found that the charge gap equals the spin gap in the Peierls insulator while  $\Delta_c > \Delta_s = 0$  in the Mott insulator, which proves spin–charge separation in the latter state.

*Note added in proof.* After this work was submitted the Tomonaga–Luttinger–liquid correlation parameter  $K_\rho$  has been determined for the half-filled spinless fermion Holstein model by DMRG, exploiting the static charge structure in the long-wavelength limit,  $K_\rho = \pi \lim_{q \rightarrow 0^+} [S_c(q)/q]$ , with  $q = 2\pi/N$  ( $N \rightarrow \infty$ ), rather than the leading-order scaling relations (1.4) and (1.5) [52]. While both approaches give almost identical results for intermediate-to-large phonon frequencies, the authors of Ref. [52] find  $K_\rho < 1$  also in the adiabatic regime, which puts the subdivision of the metallic state into an attractive and repulsive Luttinger liquid into question.

## Acknowledgements

We thank A. Alvermann, K.W. Becker, A.R. Bishop, F. Göhmann, M. Hohenadler, E. Jeckelmann, A.P. Kampf, A. Weiße and G. Wellein for valuable discussions. This work was supported by DFG through SFB 652 and KONWIHR Bavaria project HQS@HPC. Furthermore, we acknowledge generous computer granting by LRZ Munich and HLRN Berlin.

## References

1. N.F. Mott, *Metal-Insulator Transitions* (Taylor and Francis, London, 1990)
2. R. Peierls, *Quantum theory of solids* (Oxford University Press, Oxford, 1955)
3. N. Tsuda, K. Nasu, A. Yanase, K. Siratori, *Electronic Conduction in Oxides* (Springer, Berlin, 1990)
4. A.R. Bishop, B.I. Swanson, *Los Alamos Sci.* **21**, 133 (1993)
5. Y. Takada, A. Chatterjee, *Phys. Rev. Lett.* **67**, 081102(R) (2003)
6. H. Fehske, G. Wellein, G. Hager, A. Weiße, A.R. Bishop, *Phys. Rev. B* **69**, 165115 (2004)
7. M. Capone, G. Sangiovanni, C. Castellani, C. Di Castro, M. Grilli, *Phys. Rev. Lett.* **92**, 106401 (2004)
8. G.S. Jeon, T.H. Park, J.H. Han, H.C. Lee, H.Y. Choi, *Phys. Rev. Lett.* **70**, 125114 (2004)
9. R.T. Clay, R.P. Hardikar, *Phys. Rev. Lett.* **95**, 096401 (2005)
10. M. Tezuka, R. Arita, H. Aoki, *Phys. Rev. Lett.* **95**, 226401 (2005)
11. T. Holstein, *Ann. Phys. (N.Y.)* **8**, 325 (1959)
12. J. Hubbard, *Proc. R. Soc. Lond. Ser. A* **277**, 237 (1964)
13. J.K. Cullum, R.A. Willoughby, *Lanczos Algorithms for Large Symmetric Eigenvalue Computations*, vol. I and II (Birkhäuser, Boston, 1985)
14. A. Weiße, G. Wellein, A. Alvermann, H. Fehske, *Rev. Mod. Phys.* **78**, 275 (2006)
15. S.R. White, *Phys. Rev. Lett.* **69**, 2863 (1992)
16. E. Jeckelmann, H. Fehske, *Riv. Nuovo Cimento* **30**, 259 (2007)
17. H. Fehske, A. Weiße, R. Schneider, (Eds.), *Computational Many-Particle Physics*, vol. 739 (Springer, Berlin Heidelberg, 2008)
18. J.E. Hirsch, E. Fradkin, *Phys. Rev. B* **27**, 4302 (1983)
19. G. Benfatto, G. Gallavotti, J.L. Lebowitz, *Helv. Phys. Acta* **68**, 312 (1995)
20. H. Zheng, D. Feinberg, M. Avignon, *Phys. Rev. B* **39**, 9405 (1989)
21. H. Fehske, M. Holicki, A. Weiße, in *Advances in Solid State Physics 40*, ed. by B. Kramer (Vieweg, Wiesbaden, 2000), pp. 235–249
22. R.H. McKenzie, C.J. Hamer, D.W. Murray, *Phys. Rev. B* **53**, 9676 (1996)
23. R.J. Bursill, R.H. McKenzie, C.J. Hamer, *Phys. Rev. Lett.* **80**, 5607 (1998)
24. G. Wellein, H. Fehske, *Phys. Rev. B* **58**, 6208 (1998)
25. S. Sykora, A. Hübsch, K.W. Becker, G. Wellein, H. Fehske, *Phys. Rev. B* **71**, 045112 (2005)
26. M. Hohenadler, G. Wellein, A.R. Bishop, A. Alvermann, H. Fehske, *Phys. Rev. B* **73**, 245120 (2006)
27. F.D.M. Haldane, *Phys. Rev. Lett.* **45**, 1358 (1980)
28. S. Tomonaga, *Prog. Phys. Ther.* **5**, 544 (1950)

29. J.M. Luttinger, *J. Math. Phys.* **4**, 1154 (1963)
30. J.L. Cardy, *J. Phys. A* **17**, L385 (1984)
31. H. Fehske, G. Wellein, G. Hager, A. Weiße, K.W. Becker, A.R. Bishop, *Phys. B* **359-361**, 699 (2005)
32. E. Jeckelmann, F. Gebhard, F.H.L. Essler, *Phys. Rev. Lett.* **85**, 3910 (2000)
33. E. Jeckelmann, *Phys. Rev. Lett.* **89**, 236401 (2002)
34. D. Sénéchal, D. Perez, D. Plouffe, *Phys. Rev. B* **66**, 075129 (2002)
35. C.E. Greffield, G. Sangiovanni, M. Capone, *Eur. Phys. J. B* **44**, 175 (2005)
36. E. Jeckelmann, C. Zhang, S.R. White, *Phys. Rev. B* **60**, 7950 (1999)
37. H. Fehske, A.P. Kampf, M. Sekania, G. Wellein, *Eur. Phys. J. B* **31**, 11 (2003)
38. W. Kohn, *Phys. Rev.* **133**, A171 (1964)
39. A.A. Ovchinnikov, *Sov. Phys. JETP* **30**, 1160 (1970)
40. H. Fehske, G. Wellein, A. Weiße, F. Göhmann, H. Büttner, A.R. Bishop, *Phys. B* **312-313**, 562 (2002)
41. N. Gidopoulos, S. Sorella, E. Tosatti, *Eur. Phys. J. B* **14**, 217 (2000)
42. H. Fehske, G. Hager, E. Jeckelmann, *Europhys. Lett.* **84**, 57001 (2008)
43. J.W. Bray, H.R. Hart Jr., L.V. Interrante, I.S. Jacobs, J.S. Kasper, G.D. Watkins, S.H. Wee, J.C. Bonner, *Phys. Rev. Lett.* **35**, 744 (1975)
44. M. Hase, I. Terasaki, K. Uchinokura, *Phys. Rev. Lett.* **70**, 3651 (1993)
45. K. Kuboki, H. Fukuyama, *J. Phys. Soc. Jpn.* **56**, 3126 (1987)
46. A. Weiße, G. Wellein, H. Fehske, *Phys. Rev. B* **60**, 6566 (1999)
47. C. Raas, A. Bühler, G.S. Uhrig, *Eur. Phys. J. B* **21**, 369 (2001)
48. R.J. Bursill, R.H. McKenzie, C.J. Hamer, *Phys. Rev. Lett.* **83**, 408 (1999)
49. G. Hager, A. Weiße, G. Wellein, E. Jeckelmann, H. Fehske, *J. Magn. Magn. Mater.* **310**, 1380 (2007)
50. K. Okamoto, K. Nomura, *Phys. Lett. A* **169**, 433 (1992)
51. A. Weiße, G. Hager, A.R. Bishop, H. Fehske, *Phys. Rev. B* **74**, 214426 (2006)
52. E. Ejima, H. Fehske, *Europhys. Lett.* **87**, 27001 (2009)